1   Revision 1

2

3   **Jianshuiite in oceanic manganese nodules at the Paleocene-**

4   **Eocene Boundary**

5

6   **Jeffrey E. Post[1*], Ellen Thomas[2], and Peter J. Heaney[3]**

7

8

9   [1]*Department of Mineral Sciences, Smithsonian Institution, PO Box 37012, Washington, DC*

10   *20013-7012, United States*

11   [2]*Department of Geology and Geophysics, Yale University,* PO Box 208109, New Haven CT 06520

12   *United States and Department of Earth and Environmental Sciences, Wesleyan University, 265*

13   *Church Street, Middletown CT 06459*

14   [3]*Department of Geosciences, Penn State University, University Park, PA 16802, United States*

15

16

17

18   [*]*To whom correspondence should be addressed:* postj@si.edu

19

22

23   **ABSTRACT**

24   Synchrotron powder X-ray diffraction and scanning electron microscopy examinations of

25   manganese oxide concretions/nodules (~0.3 - 1.0 mm diameter) from ODP Site 1262 on Walvis

26   Ridge in the Southeastern Atlantic Ocean revealed that they consist primarily of the layered Mn

27   oxide phase jianshuiite [$(Mg,Mn,Ca)Mn^{4+}_3O_7·3H_2O$]. The nodules are from an interval with

28   severe carbonate dissolution that represents the Paleocene/Eocene (P/E) thermal maximum (~

29   55.8 Ma). Most nodules from the middle of the carbonate dissolution interval contain internal

30   open space, and consist almost entirely of euhedral plate-like jianshuiite crystals, 2-4 um in

31   diameter and ~0.1-0.5 um thick. Backscattered electron images and energy dispersive X-ray

32   analyses revealed stacks of interleaved Al-rich and Al-poor jianshuiite crystals in some nodules.

33   The crystals in other nodules contain predominantly Mg (with trace K and Al) in addition to Mn

34   and O, making them near "end-member" jianshuiite. Rietveld refinements in space group R-3

35   confirmed the isostructural relationship between jianshuiite and chalcophanite, with Mg

36   occupying the interlayer position above and below the vacant sites in the Mn/O octahedral sheet,

37   and coordinated to 3 octahedral layer O atoms (1.94 Å) and 3 interlayer water O atoms (2.13 Å).

38   Final refined occupancy factors suggest that small quantities of Ni and possibly Mn^{2+} are located

39   on the Mg site. The transient appearance of the Mg-rich birnessite-like phase jianshuiite,

40   probably abiotically produced, must indicate an exceptional transient change in the chemistry of

41   the pore fluids within deep ocean sediments directly following the P/E boundary, possibly as a

42   result of decreasing oxygen levels and pH, followed by a return to pre-event conditions.

43

44

INTRODUCTION

46   Site 1262 was drilled on Ocean Drilling Program Leg 208 on the northwestern flank of

47   Walvis Ridge in the Southeastern Atlantic Ocean, west of South Africa (Zachos et al. 2004).

48   Lower Cenozoic sediments at Site 1262 consist mainly of foraminifera-bearing, carbonate-rich

49   nannofossil ooze with minor clay and volcanic ash. The Paleocene/Eocene (P/E) boundary

50   occurs at an abrupt contact between nannofossil ooze and a red clay (Zachos et al. 2005;

51   McCarren et al., 2008) (Fig. 1). This clay layer corresponds to a period of severe carbonate

52   dissolution at the onset of the most extreme global warming event in the Cenozoic, the

53   Paleocene/Eocene Thermal Maximum (PETM), dated at ~55.8 Mya (e.g., McInerney and Wing

54   2012; Dunkley-Jones et al. 2013). The warming was triggered by a massive injection of

55   isotopically light carbon into the ocean - atmosphere system (e.g., Dickens et al. 1995; Thomas

56   and Shackleton 1996). The source of the carbon, its nature (CH_4 or CO_2 or a mixture), and the

57   mechanisms and duration of release are still debated (McInerney and Wing 2012; Dickens 2011;

58   Dunkley-Jones et al., 2013). The strong increase in atmospheric pCO_2 caused by the release of

59   thousands of gigatons of carbon compounds over less than 10,000 yr caused global warming by

60   5-8 ^{o}C (Dunkley-Iones et al., 2013) and severe ocean acidification, and these events in turn led to

61   an abrupt shallowing of the carbonate compensation depth (Zachos et al. 2005; Ridgwell and

62   Schmidt, 2010; Hoenisch et al., 2012; Winguth et al. 2012).

63   The >38 um size fraction of the sediment in the carbonate-free section at Site 1262

64   (paleodepth ~3500 m; Zachos et al. 2005; Foster et al. 2013) consists primarily of Mn oxide

65   "nodules", along with fish detritus (Fig. 2a). The nodules measure ~1-5 mm or smaller in

66   diameter. They comprise only a minor fraction of the bulk sediment, with only <1 wt. % of the

67   bulk sediment in the > 38 um size fraction. The concentration of Mn in the bulk clay layer is ~20

68    $\mu mol/g^{-1}$ (Chun et al. 2010).

69   For this study, we investigated the mineralogy of the Mn nodules in the sedimentary

70   record at Site 1262 as well as similar nodules at other sites on Walvis Ridge (e.g., Site 1265,

71   Zachos et al. 2004). Our analyses of the nodules from the PETM clay interval at Site 1262

72   revealed the predominance of jianshuiite, a Mg-rich phyllomanganate, with unusually high

73   crystallinity. For the first time, we present a full structure refinement and characterization of this

74   rare Mn oxide mineral. Since the PETM represents an extreme climatic anomaly in the

75   Cenozoic, unusual minerals within the sediments associated with this event, and their geographic

76   and bathymetric occurrence, may provide important clues to explain the origin of the warming

77   episode.

78

79   **EXPERIMENTAL DETAILS**

80   **Sample selection**

81   All samples were taken from cores collected during Ocean Drilling Program Leg 208

82   (March-May 2003) (Zachos et al. 2004). Cores were treated following standard procedure on

83   Ocean Drilling expeditions, i.e., they were split, described and photographed on-board ship. The

84   Mn-nodules were noted during core description onboard ship (Zachos et al. 2004). The core

85   halves were designated as archive half and working half, and placed in plastic D-tubes, with the

86   sediment kept moist by inserting a sponge before closing and taping the D-tube. Cores were kept

87   in cold storage space on the ship, during transport and in the core repository. Some samples were

88   taken onboard ship, others during sampling at the Bremen (Germany) core repository from the

89   working half of the core several months after the cruise. Samples were freeze-dried and wet-

90   sieved following standard paleoceanographic procedure (e.g., McCarren et al. 2008). The

91   nodules were hand-picked from the >38 um sieve fraction using a binocular microscope. The

92   individual samples were small (slices 1 cm thick, McCarren et al. 2008), and all nodules were

93   picked from the samples.

94   Twelve nodules were examined from the >38 um sieve fraction recovered from Site 1262

95   ($27^o11.15$'S, $01^o34.62$'E; water depth 4755m), Hole B, Core 15H, Section 3, from the ~30 cm

96   interval above the P/E contact (Fig. 1), ranging from the bottom to the top of that interval. We

97   also studied similar looking nodules, in size and shape, from older and younger sediments in

98   cores from Site 1262 and nearby Site 1265 ($28^o50.10$'S, $02^o38.35$'E, depth 3060 m), including:

99   1262A-4H (Miocene), 1265A-27H (lower Eocene), 1265A-18H (lower Oligocene), and 1262A-

100   17H (mid-Paleocene). We looked for nodules at the shallowest site drilled on Walvis Ridge, Site

101   1263, which also contains an interval of severe carbonate dissolution across the PETM (Zachos

102   et al. 2005), but the carbonate-free sediments do not contain Mn-oxide nodules. Mn may be

103   present as Mn-carbonate (Chun et al. 2010).

104

105   **Sample characterization**

106   **Scanning electron microscopy.** We performed analytical scanning electron microscopy (SEM)

107   using an FEI Nova NanoSEM 600 with a Thermo Ultradry Silicon drift energy dispersive X-ray

108   detector in the Department of Mineral Sciences, Smithsonian Institution. The nodules were

109   mounted onto carbon tape on a carbon stub; back-scattered electron imaging and energy

110   dispersive spectroscopy (EDS) analyses were carried out on uncoated samples using the low

111   vacuum mode and 15 keV accelerating voltage.

112   **X-ray diffraction and crystallographic analysis.** We used both conventional and synchrotron

113   powder X-ray diffraction to characterize the minerals in the Mn-oxide nodules from the PETM-

114   clay interval at Site 1262. Initial sample identification was performed using a Rigaku D-MAX

115   Rapid microdiffractometer with Mo $K\alpha$ radiation and an imaging plate detector. For these

116   experiments, a ~1 mm nodule (from ~11 cm above the P/E contact) was mounted with super glue

117   onto a glass fiber and rotated 1° per second during powder diffraction data collection. The

118   synchrotron X-ray diffraction data from the same nodule were collected at beamline 13-BM-C (λ

119   = 0.8265(8) Å; CCD detector radius = 95.165 mm) at the Advanced Photon Source (APS),

120   Argonne National Laboratory (ANL), using an exposure time of 30 s. The small, and uniform,

121   jianshuiite crystallite sizes and their "random" arrangement within the nodule provided for good

122   quality diffraction data. Although none was obvious, any possible preferred orientation of the

123   powder was eliminated by full intensity integration of the diffraction rings, as obtained using the

124   program Fit2D (Hammersley et al. 1996) with a polarization factor of 0.99.

125   Rietveld refinements were performed using the general structure analysis system (GSAS)

126   of Larson and Von Dreele (2006) and EXPGUI interface by Toby (2001). The starting jianshuiite

127   structural parameters were taken from the isostructural chalcophanite structure reported by Post

128   and Appleman (1988). Difference-Fourier maps were calculated using the MnO octahedral layers

129   in order to locate the Mg atoms and water molecules in the interlayer region. The diffraction

130   pattern backgrounds were fit using a linear interpolation function. Peak profiles were modeled by

131   a pseudo-Voigt profile function as parameterized by Thompson et al. (1987) with asymmetry

132   corrections by Finger et al. (1994) and microstrain anisotropic broadening terms by Stephens

133   (1999).

134   During the initial cycles of refinement, only the background, scale, peak profile, and unit-

135   cell parameters were allowed to vary. After convergence, all atom positions, displacement

136   factors, and appropriate occupancy factors (e.g. of the Mg and Mn sites) were refined.

137   Difference patterns revealed a small amount of quartz in the sample, consistent with SEM

138   observations. Rietveld refinement that included quartz improved the fit and revealed its

139   abundance as less than 2 wt% of the sample.

140

141   **RESULTS**

142   **Nodule characterization by microscopy**

143   The Mn-rich nodules from the clay interval at Site 1262 typically were dark brown and

144   ovoid, ranging in length from ~0.3 to ~1 mm along the longest axis. Most of the nodules

145   contained an internal open space (Fig. 2a) with walls measuring ~100 um in thickness. The sizes

146   and shapes of the hollow nodules were not obviously suggestive of pseudomorphism after a

147   precursor mineral or organism, such as foraminiferal tests (B. Huber, pers. comm.), but some

148   could have been pseudomorphs of fecal pellets.

149   Back-scattered electron images at high magnification revealed that the nodule walls

150   consist of euhedral crystals with apparently hexagonal symmetry, measuring 3-5 um across, with

151   a thickness of 0.1 to 1 um (Fig. 2b). Because of the small size of the crystals, it was not possible

152   to obtain quantitative electron microprobe analyses, but EDS analyses of the crystals showed

153   predominantly Mn and O, with Mg and various amounts of Al, and minor K, Ca, Ba, Si, Ni and

154   Co. These analyses led to an initial identification of the material composing the nodular walls as

155   the magnesian birnessite-like phase jianshuiite: $MgMn^{4+}_3O_7 \cdot 2.80\ H_2O$ (Guiyin et al. 1992).

156   Some of the jianshuiite crystals (Fig. 3a,b) appear to have separated into thin layers, reminiscent

Page 7

157   of a vermiculite crystal that swells and expands upon heating. EDS analyses of the expanded

158   regions showed higher concentrations of Ca, K and Ba, and less Al and Ni, than did the more

159   compacted portions of the crystals (Fig. 3a).

160   Although micronodules that were apparently similar in shape, color and size were

161   observed throughout the cores of several sites drilled on Walvis Ridge (Zachos et al., 2004), the

162   jianshuiite crystals were observed only in nodules from within the horizon immediately above

163   the P/E boundary, corresponding to the Core 1262A-15H-3 interval between ~73 and 40 cm,

164   where carbonate dissolution was greatest. We examined by SEM/EDS five nodules that spanned

165   this interval and observed variations in the proportions of carbonate nannofossils and Mn oxides,

166   and in the type of Mn oxide.

167   A nodule from ~1 cm above the P/E contact contained numerous carbonate nannofossils

168   and other mineral grains, including clays, such as illite, quartz and barite. The jianshuiite crystals

169   in this nodule were subhedral to rarely euhedral in shape. A nodule from ~9 cm above the

170   contact was devoid of carbonates, and it consisted predominantly of euhedral jianshuiite, but

171   many of the crystals were exfoliated into thin layers that were more K- and Ca- rich than the bulk

172   jianshuiite (Fig. 3a, b). A nodule from ~11 cm above the contact was composed almost entirely

173   of euhedral jianshuiite crystals, with scattered grains of quartz and K- and Mg-rich silicates

174   (likely clays) and apatite. This nodule was used for our crystal structure refinement of

175   jianshuiite. In a nodule from 22 cm above the P/E boundary, carbonate nannofossils reappear,

176   and euhedral jianshuiite crystals line vugs and the interior cavity wall. A nodule from 32 cm

177   above the contact contained abundant carbonate nannofossils with euhedral jianshuiite crystals in

178   small cavities and vugs (Fig. 4).

Page 8

179   We also examined several nodules from other cores at Site 1262 and nearby Site 1265

180   that were recovered from sediments older and younger than the PETM. These nodules exhibited

181   comparable sizes and shapes as those from the PETM described above, but appeared to the eye

182   to be lighter colored. SEM images revealed that they consisted predominantly of carbonate

183   nannofossils, and minor Ca-rich Mn oxides, likely todorokite (Fig. 5). Jianshuiite was only

184   observed in the nodules from the PETM horizon in Core 1262B-15H-3.

185

186   **XRD identification of jianshuiite**

187   **Chalcophanite and jianshuiite.**   Powder X-ray diffraction patterns collected from individual

188   nodules in the carbonate dissolution interval associated with the PETM in Section 1262B-15H-3

189   revealed minor amounts of quartz, illite, and other clays, but the dominant mineral belonged to

190   the family of 7-Å birnessite-like phases with hexagonal symmetry. The chalcophanite

191   ($ZnMn^{4+}_3O_7 \cdot 3H_2O$) structure (Wadsley 1955; Post and Appleman 1988; Post and Heaney 2014)

192   offered a close match. However, the EDS analyses revealed that Mg rather than Zn was the most

193   abundant cation after Mn, confirming that the primary phase composing the nodules was nearly

194   end-member jianshuiite.

195   Chalcophanite originally was indexed to a triclinic cell (Wadsley 1955), and because the

196   powder X-ray diffraction pattern for jianshuiite closely resembles that of chalcophanite, Guiyin

197   et al. (1992) first described jianshuiite as a triclinic structure with Mg as the dominant interlayer

198   cation. Their wet chemical analyses yielded the following formulas for two samples:

199    $(Mg_{0.51}Mn_{0.44} Ca_{0.08})Mn^{4+}_{3.03}O_{7.1} \cdot 2.90H_2O$ and $(Mg_{0.85}Mn_{0.05})Mn^{4+}_{3.15}O_7 \cdot 2.80H_2O$. Our chemical

200   analyses of jianshuiite from the PETM cores are consistent with the near end-member jianshuiite

201   composition, but indexing of the powder diffraction pattern and subsequent structure refinement

202   has suggested a different symmetry for this mineral. We report here the first complete crystal

203   structure for jianshuiite, and in the correct trigonal unit cell.

204   The parameters determined by our Rietveld refinement using the synchrotron X-ray

205   diffraction data for jianshuiite are listed in Table 1. Atom positions are reported in Table 2, and

206   selected bond distances are reported in Table 3. The final observed, calculated, and difference

207   patterns for the Rietveld refinement using the synchrotron data are plotted in Figure 6. The

208   standard deviations calculated by GSAS for the lattice parameters are likely smaller than the true

209   errors (Post and Bish 1989).

210   As with chalcophanite (Post and Appleman, 1988), we refined jianshuiite in space group

211   R -3. One out of every seven octahedral sites in the Mn-O sheet was vacant. The Mg (Zn in

212   chalcophanite) cations were located above and below the vacancies. The vacant Mn sites were

213   fully ordered. The Mn^{4+}-O octahedra were distorted, with bond distances ranging from 1.85 to

214   2.00 Å in jianshuiite, caused by displacement of Mn toward the vacancy in the octahedral sheet;

215   in chalcophanite, the distances range from 1.86 to 1.97 Å (Post and Appleman, 1988). The mean

216   Mn-O distance for jianshuiite (Table 3) was 1.93 Å, slightly larger than the value of 1.91 Å

217   reported for chalcophanite, but still indicating that the Mn is tetravalent (Shannon 1976).

218

219   **Interlayer structure.** Our refinements indicated that Mg cations (and minor Ca and possible

220   Mn^{2+} cations) occupy sites above and below the vacancies in the octahedral sheets and are

221   coordinated to three O atoms and three water oxygen atoms. The mean Mg-O distance was 2.03

222   Å; as is the case for Zn in chalcophanite, the Mg-O bonds to the water oxygen atoms were longer

223   (2.13 Å) than those to the O atoms in the octahedral layer (1.94 Å). By analogy with

224   ernienickelite – the Ni-rich structural analog to chalcophanite (Grice et al. 1994) – the trace Ni

225   cations revealed by EDS likely are located on the Mg site, perhaps accounting for the

226   observation that the refined occupancy factor for Mg exceeded unity [Mg_{occ} = 1.07(1)]; Co,

227   however, likely substitutes for some of the octahedral Mn^{4+} (Manceau et al. 1992).

228   Unfortunately, the limitations in our chemical analyses, the small quantities of minor elements,

229   and the similarity of X-ray scattering factors among Mn, Ni and Co make definitive site

230   assignments impossible. Because Ba is significantly larger than Mg [crystal radii of 1.49 vs. 0.86

231   Å (Shannon 1976)], it is likely that any Ba is located closer to the center of the interlayer region,

232   as is the case in synthetic Ba-rich birnessite-like phases (Lopano et al. 2007).

233

234   **DISCUSSION**

235   **Other occurrences of jianshuiite**

236   Guiyin et al. (1992) named jianshuiite after its locality (Lu Village, Janshui County, Yunnan

237   Province, China), where they observed it as a hypogene phase associated with terrestrial

238   manganese ores. Another reported occurrence is in the Ojos Negros iron mines near Aragón

239   Spain (Calvo 2008). As part of a paleomagnetic study of upper Paleocene silty red sediments in

240   Baja California, Larson and Walker (1975) characterized locally abundant Mn-rich concretions

241   with major concentrations of Mg and Ba, and minor Fe, Al, Ca, and Ti. Their low analytical

242   totals suggested that the phase contained a significant amount of water. The mineral was

243   informally named "hydropsilomelane". Potter and Rossman (1979) analyzed this material using

244   X-ray powder diffraction and infrared spectroscopy, and they concluded that the Mn oxide phase

245   had the chalcophanite structure. Using Larson and Walker's (1975) analytical data, they

246   calculated the chemical formula as $(Mg_{0.6}Ba_{0.1}Fe_{0.1})$ $(Mn_{3.0}Al_{0.1})$ $\cdot 2H_2O$, and proposed that

247   "hydropsilomelane" is, in fact, a Mg analogue of chalcophanite. Although they did not formally

Page 11

248   recognize it as a new mineral, this work first reported the Mn oxide phase later described as

249   jianshuiite. In addition, Jianshuiite was identified by XRD as a minor phase in ferromanganese

250   nodules in Miocene carbonate-mud mounds in the Gulf of Cadiz (Gonzalez et al. 2009, 2012).

251   The authors argue that ferromanganese minerals including siderite-rhodochrosite grew

252   diagenetically, fueled by anaerobic oxidation of thermogenic hydrocarbons, and were replaced

253   by Fe-Mn oxyhydroxides when seawaters became more oxygen-rich, possibly microbially

254   induced.

255
256   **Jianshuiite formation and implications for changes in Eh and/or pH in PETM pore waters**

257   The jianshuiite nodules observed within the PETM clay layer differ fundamentally from

258   superficially similar micronodules in older and younger sediments, which contain mainly

259   carbonate material and some minor Mn oxide phases, likely todorokite. The ocean and/or pore

260   water conditions during the PETM at Site 1262 differed from those during other time periods,

261   specifically in a lower pH (i.e., lower carbonate saturation, Ω, leading to the dissolution of

262    $CaCO_3$; Zachos et al. 2005; Foster et al., 2013) and higher temperatures (McCarren et al. 2008).

263   Before and shortly after the PETM, the bottom waters at the depth of Site 1262 were generally

264   well-oxygenated, but at the PETM itself, oxygen levels might have decreased (Chun et al.,

265   2010). Climate modeling generally agrees with the geochemical data, indicating lowered oxygen

266   in the SE Atlantic due to temperature rise and circulation changes (e.g., Winguth et al. 2012). It

267   is not clear whether a decreased delivery of organic matter to the sea floor, and thus decreased

268   oxidation of organic matter, could have counteracted the tendency toward lower oxygen levels

269   (Ma et al. 2014).

270   The behavior of Mn in pore waters in Pleistocene-Recent sediments at a Walvis Ridge

271   location close to that from which the present PETM cores were taken, was studied by Gingele

272   and Kasten (1994). In general, dissolved Mn^{2+} migrates upward in sediment pore waters to the

273   oxic/suboxic boundary, where it oxidizes and precipitates, unless the supply of organic matter

274   atop the seafloor is sufficiently high that the bottom ocean waters are reduced (Mangini et al.

275   2001). Chun et al. (2010) argued that reducing conditions characterized the onset of the PETM,

276   and could have mobilized Mn as Mn^{2+}. The Mn in jianshuiite is in the 4+ oxidation state. Thus,

277   the precipitation of jianshuiite may represent a diagenetic event that occurred once oxidizing

278   conditions returned later – either during or after the main part of the PETM, possibly similar to

279   the sequence of events reported by Gonzalez et al. (2012). Mn oxide nodules are absent at

280   shallower Site 1263, because conditions there were less oxidizing than at Site 1262 before,

281   during and after the PETM (Chun et al. 2010). The formation of chalcophanite may provide an

282   analogous genetic pathway, since it forms in Zn-rich oxidized zones of terrestrial Mn-rich

283   deposits. Mn oxidation can also occur at constant solution Eh through a rise in pH (e.g., Takeno

284   2005), and therefore, the transition from dissolved Mn^{2+} to Mn^{4+} might have resulted from an

285   increase in pH of pore waters after the acidification event at the P/E boundary ended.

286   Any carbonate phases in the Walvis Ridge sediments (derived from the pelagic calcifyers

287   in the surface waters) would have dissolved early in the PETM, potentially leaving sediment

288   pore space and voids. The nodule morphology might be attributed to the growth of jianshuiite

289   crystals on cavity walls, as Mn in the pore fluid was oxidized, forming a hollow shell such as that

290   in Figure 2a. Alternatively, the jianshuiite might have crystallized on the walls of burrows, or

291   on the outside of fecal pellets, or of calcareous tests that later dissolved. Previous studies (Chun

292   et al. 2010; Paelike et al. 2014) suggest that carbonate dissolution preceded the reoxidation, so

293   calcareous tests dissolved long before oxic fluids would have precipitated dissolved Mn. This

Page 13

294   consideration might support the hypothesis that increases in pore water pH induced the

295   precipitation of jianshuiite during a later diagenetic event.

296

297   Jianshuiite formation and implications for high Mg/Ca ratios in PETM pore waters

298   One of the most intriguing aspects of the PETM Mn nodules is that they are composed of

299   well-formed microcrystals of the rare Mn oxide mineral jianshuiite. In contrast, the macroscopic

300   Mn nodules that cover broad expanses of the ocean floor (and occur in core samples at Walvis

301   Ridge in older and younger sediments than the PETM) contain phases such as todorokite

302    $[(Na,Ca,K)_2 (Mn^{4+},Mn^{3+})_6 O_{12} \cdot 3\text{-}4.5H_2O]$, "buserite" $(Na_4Mn_{14}O_{27} \cdot 21H_2O)$, and vernadite

303    $[(Mn^{4+},Fe^{3+},Ca,Na)(O,OH)_2 \cdot nH_2O]$ (Burns and Burns 1977). Moreover, most researchers have

304   concluded that the precipitation of Mn oxides in seafloor nodules is biologically mediated (e.g.,

305   Moffett and Ho 1996; Tebo et al. 2004), and these biogenic Mn oxides invariably are fine-

306   grained and poorly crystalline, as is the jianshuiite in the nodules described by Gonzalez et al.

307   (2009, 2012). The strongly euhedral nature and relatively large sizes of the jianshuiite crystals in

308   the PETM nodules are atypical of known synthetic or natural biogenic Mn oxides.

309   Consequently, we infer that the PETM nodules formed abiotically, possibly induced by the

310   unusually severe changes in oxygenation and pH during the PETM, although organisms or other

311   organic material in the sediments might have contributed to the particular chemical conditions

312   that resulted in the formation of the jianshuiite crystals.

313   The high concentration of Mg relative to Ca in jianshuiite would seem to reflect pore

314   water chemistries in PETM sediments that contained anomalously high Mg/Ca ratios, especially

315   because Mg/Ca values in seawater at the time of the PETM may have been much lower than

316   today (e.g., Stanley and Hardie 1998; Farkas et al. 2007). The transient nature of this high-

Page 14

317   magnesian pulse is evidenced by the return of organisms with Ca carbonate tests, such as

318   foraminifera and nannofossils, higher in the section.

319   Intriguingly, the jianshuiite crystals themselves might record changes in the Mg/Ca

320   compositions of fluids through cation-exchange textures that are observable in some crystals.

321   We have documented previously that Cs exchange within the interlayer of Na-birnessite occurs

322   through a delamination-relamination ("delam-relam") mechanism rather than through classic

323   dissolution-reprecipitation pathways (Lopano et al. 2009; Fleeger et al. 2013). The expanded,

324   accordion-like jianshuiite crystals seen in Figure 3 provide strong textural evidence for delam-

325   relam alteration resulting from cation exchange. In the delam-relam process, cation exchange

326   between the aqueous phase and the Mn oxide interlayer occurs via the separation of individual

327   layers followed by the wholesale substitution of the interlayer cations, in contrast to traditional

328   exchange processes that occur by diffusion of substitutional cations from the surface of a crystal

329   to its interior. It seems especially significant that spot EDS analyses of these accordion-like

330   crystals reveal a consistently higher concentration of Ca to Mg in the expanded portions of the

331   crystals than in the compressed regions. The crystals showing possible exchange textures were

332   most obvious in the nodule from ~9 cm above the P/E contact, and above the last appearance of

333   calcareous nannofossils (which are still visible in the nodule 1 cm above the contact). Perhaps

334   the dissolution of carbonates resulted in a rise in Ca concentrations in pore waters (Foster et al.

335   2013) that deposited the jianshuiite, and these now Ca-rich solutions reacted with the jianshuiite

336   crystals, leading to partial cation exchange.

337

338

339

Page 15

IMPLICATIONS

340   As described by models of mineral evolution (Hazen et al. 2008), the appearance of new

341 minerals within the rock record can signify fundamental changes in events that govern Earth

342 processes. Surveys of Mn oxides within modern near-surface environments have uniformly

343 indicated the predominance of poorly crystalline, biogically precipitated Ca-rich Mn oxides, such

344 as buserite and/or rancieite ($(Ca,Mn)Mn_4O_9 \cdot 3H_2O$), vernadite, and todorokite. The transient

345 appearance of the Mg-rich birnessite-like phase jianshuiite must indicate an exceptional change

346 in the chemistry of the pore fluids within deep ocean sediments at the P/E boundary. As is

347 consistent with other transitions during this global warming event, we infer that pulses of fluids

348 with high Mg/Ca values deposited the jianshuiite within cavities formed by the prior dissolution

349 of carbonate micronodules. The tetravalent oxidation state of the Mn suggests that these

350 depositional fluids were less acidic than those that led to the abrupt carbonate dissolution event

351 at the onset of the PETM. We speculate that jianshuiite might have been mistaken for other Mn

352 oxides at other sites, and it might serve as a marker mineral for climate change events, such as

353 these recorded by Gonzalez et al. (2012).

354   Birnessite-like phases are challenging to investigate because they tend to occur as fine-

355 grained, poorly crystalline masses. Chalcophanite, and now jianshuiite, are unusual in the

356 birnessite family because they are exceptionally well-crystallized, sometimes forming crystals up

357 to several millimeters in diameter, as in the case of chalcophanite. Consequently, these phases

358 serve as excellent crystallographic proxies for the structures and chemical behaviors of the

359 broader group of birnessite-like minerals.

ACKNOWLEDGEMENTS

REFERENCES

373

374　Burns, R. G. and Burns, V. M. (1977) in *Marine Manganese Nodules*, ed. Glasby, G.P. (Elsevier,

375　　　　Amsterdam), pp. 185-248.

376　Calvo, M. (2008) Minerales de Aragón. Prames, Zaragoza. 463 pp.

377　Chun, C. O. J., M. L. Delaney, and J. C. Zachos (2010), Paleoredox changes across the

378　　　　Paleocene-Eocene thermal maximum, Walvis Ridge (ODP Sites 1262, 1263, and 1266):

379　　　　Evidence from Mn and U enrichment factors, Paleoceanography, 25 (4), PA 4202.

380　Dickens, G. R., O'Neil, J. R., Rea, D. K., and Owen, R. M. (1995) Dissociation of oceanic

381　　　　methane hydrate as a cause of the carbon isotope excursion at the end of the Paleocene,

382　　　　Paleoceanography, 19, 965–971.

383　Dickens, G. R. (2011) Down the rabbit hole: towards appropriate discussion of methane release

384　　　　from gas hydrate systens during the Paleocene-Eocene thermal maximum and other past

385　　　　hyperthermal events, Climate of the Past, 7, 831-846.

386　Dunkley Jones, T., D. J. Lunt, D. N. Schmidt, A. Ridgwell, A. Sluijs, P. J. Valdes, and M.

387　　　　Maslin (2013), Climate model and proxy data constraints on ocean warming across the

388　　　　Paleocene–Eocene Thermal Maximum, Earth-Science Reviews, 125, 123-145.

389　Fleeger, C. R., Heaney, P. J., & Post, J. E. (2013). A time-resolved X-ray diffraction study of Cs

390　　　　exchange into hexagonal H-birnessite. American Mineralogist, 98, 671-679.

391　Foster, L. C., Schmidt, D. N., Thomas, E., Arndt, S., and Ridgwell, A. (2013) Surviving rapid

392　　　　climate change in the deep-sea during the Paleogene hyperthermals. *Proc. Nat. Acad.*

393　　　　*Sci.*, 110: 9273-9276.

394　Gingele, F. X., and Kasten, S. (1994) Solid-phase manganese in Southeast Atlantic sediments:

395　　　　implications for paleoenvironments. Marine Geology, 121, 317-332.

Page 18

396   Golden, D.C., Dixon, J.B., and Chen, C.C. (1986) Ion exchange, thermal transformations, and

397   oxidizing properties of birnessite. Clays and Clay Minerals, 34, 511-520.González, F.J.,

398   Somoza, L., Lunar, R., Martínez-Frías, J., Martín Rubí, J.A., Torres, T., Ortiz, J.E., Díaz

399   del Río, V., Pinheiro, L.M., Magalhães, V.H., 2009. Hydrocarbon-derived

400   ferromanganese nodules in carbonate-mud mounds from the Gulf of Cadiz: mudbreccia

401   sediments and clasts as nucleation sites. Marine Geology, 261, 64–81.

402   González, F.J., Somoza, L.,Leon, R., Mdialdea, T., Torres, T., Ortiz, J. E., Lunar, R., Martinez-

403   Frias, J., and Merinero, R., 2012. Ferromanganese nodules and micro-hardgrounds

404   associated with the Cadiz Contourite Channel (NE Atlantic):

405   Palaeoenvironmental records of fluid venting and bottom currents, Chemical

406   Geology, 310-311, 56-78.

407   Grice, J.D. Gartrell, B., Gault, R.A. & Van Velthuizen, J. (1994): Ernienickelite,

408   NiMn3O7·3H2O, a new mineral species from the Siberia complex, Western Australia:

409   comments on the crystallography of the calcophanite group. Canadian Mineralogist 32,

410   333-337.

411   Guiyin, Y., Shanghua, Z., Mingkai, Z., Jianping, D. and, Deyu, L. (1992): Jianshuiite - A new

412   magnesic mineral of chalcophanite group. Acta Mineralogica Sinica 12(1), 69-77. (in

413   Chinese with English abstract)

414   Hammersley, A.P., Svensson, S.O., Hanfland, M., Fitch, A.N., and Hausermann, D. (1996) Two-

415   dimensional detector software: From real detector to idealized image or two-theta scan.

416   High Pressure Research, 14, 235–248.

417   Hazen, R. M., Papineau, D., Bleeker, W., Downs, R. T., Ferry, J. M., McCoy, T. J., Sverjensky,

418   D.M., and Yang, H. (2008). Mineral evolution. American Mineralogist, 93, 1693-1720.

419   Johnson E.A. and Post, J.E. (2006) Water in the interlayer region of birnessite: importance in

420   cation exchange and structural stability. American Mineralogist, 91, 609-619.

421   Jones, L.H.P. and Milne, A.A. (1956) Birnessite, a new manganese oxide mineral from

422   Aberdeenshire, Scotland. Mineralogical Magazine, 31(235), 283-288.

423   Kwon, K.D., Refson, K. and Sposito, G. (2009) Zinc surface complexes on birnessite: A density

424   functional theory study. Geochimica et Cosmochimica Acta, 73, 1273-1284.

425   Larson, A.C., and Von Dreele, R.B. (2006) GSAS-General Structure Analysis System. Los

426   Alamos National Laboratory Report, LAUR 86-748.

427   Lopano, C.L., Heaney, P.J., Post, J.E., Hanson, J., and Komarneni, S. (2007) Time-resolved

428   structural analysis of K- and Ba-exchanged reactions with synthetic Na-birnessite using

429   synchrotron X-ray diffraction. American Mineralogist, 92, 380-387.

430   Lopano, C.L., Heaney, P.J., and Post, J.E. (2009) Cs-exchange in birnessite: Reaction

431   mechanisms inferred from time-resolved X-ray diffraction and transmission electron

432   microscopy. American Mineralogist, 94, 816-826.Ma, Z., Gray, E., Thomas, E., Murphy,

433   B., Zachos, J. C., and Paytan, A. (2014) Carbon sequestration during the Paleocene-

434   Eocene Thermal maximum by an efficient biological pump. Nature Geoscience 7: 382-

435   388.

436   Manceau, A., Gorshkov, A. I., and Drits, V. A. (1992) Structural chemistry of Mn, Fe, Co, and

437   Ni in manganese hydrous oxides: Part II. Information from EXAFS spectroscopy and

438   electron and X-ray diffraction. American Mineralogist, 77, 1144-1157.

439   Mangini, A., Jung, M., and Luakenmann, S., 2001. What do we learn from peaks of uranium and

440   of manganese in deep-sea sediments? Marine Geology, 177, 63-78.

441   McCarren, H., Thomas, E., Hasegawa, T., Roehl, U., and Zachos, J. C. (2008) Depth-

442   dependency of the Paleocene-Eocene Carbon Isotope Excursion: paired benthic and

443   terrestrial biomarker records (ODP Leg 208, Walvis Ridge). Geochemistry, Geophysics,

444   Geosystems, **9 (10):** Q10008, doi: 10.1029/2008GC002116

445   McInerney, F. A., and Wing, S. L. (2011), The Paleocene-Eocene Thermal Maximum: A

446   Perturbation of Carbon Cycle, Climate, and Biosphere with Implications for the Future,

447   Annual Review of Earth and Planetary Sciences, Vol. 39, edited by R. Jeanloz and K. H.

448   Freeman, pp. 489-516.

449   McKenzie, R.M. (1976) The manganese oxides in soils. In I.M. Varentsov, and G. Grasselly,

450   Eds. Proceedings of the 2nd International Symposium on Geology and Geochemistry of

451   Manganese, 1, p. 259-269. Schweizerbart, Stuttgart.

452   McKenzie, R.M. (1977) Manganese oxides and hydroxides. In J.B. Dixon, and S.B. Weed, Eds.

453   Minerals in Soil Environments, p. 181-193. Soil Science Society of America, Madison,

454   Wisconsin.

455   Moffett, J. W., and Ho, J. (1996) Oxidation of cobalt and manganese in seawater via a common

456   microbially mediated pathway. Geochimica et Cosmochimica Acta 60 (18): 3415-3424.

457   Post, J.E. and Appleman, D.E. (1988) Chalcophanite, $ZnMn_3O_7 \cdot 3H_2O$: New crystal-structure

458   determinations. American Mineralogist, 73, 1401-1404.

459   Post, J.E., and Bish, D.L. (1989) Rietveld refinement of crystal structures using powder X-ray

460   diffraction data. In D.L. Bish and J.E. Post, Eds., Modern Powder Diffraction, 20, p. 277-

461   308. Reviews in Mineralogy, Mineralogical Society of America, Chantilly, Virginia.

462   Post, J.E. (1999) Manganese oxide minerals: Crystal structures and economic and environmental

463   significance. Proceedings of the National Academy of Sciences, 96, 3447-3454.

464   Post, J.E. and Heaney, P.J. (2014) Time-resolved synchrotron X-ray diffraction study of the

465   dehydration behavior of chalcophanite. American Mineralogist, 99, 1956-1961.

466   Post, J.E., Heaney, P.J., and Ertl, A. (2008) Rietveld refinement of the ranciéite structure using

467   synchrotron powder diffraction data. Powder Diffraction, 23, 10-14.

468   Potter, R.M. and Rossman, G.R. (1979) Mineralogy of manganese dendrites and coatings.

469   American Mineralogist, 64, 1219-1226.

470   Ridgwell, A., and Schmidt, D. N., (2010) Past constraints on the vulnerability of marine

471   calcifiers to massive carbon dioxide release. Nature Geoscience, 3, 196-200.

472   Shannon, R.D. (1976) Revised effective ionic radii and systematic studies of interatomic

473   distances in halides and chalcogenides. Acta Crystallographica, A32, 751-767.

474   Silvester, E., Manceau, A., and Drits, V. (1997) Structure of synthetic monoclinic Na-rich

475   birnessite and hexagonal birnessite: II. Results from chemical studies and EXAFS

476   spectroscopy. American Mineralogist, 82, 962-978.

477   Stephens, P.W. (1999) Phenomenological model of anisotropic peak broadening in powder

478   diffraction. Journal of Applied Crystallography, 32, 281–289.

479   Takeno, N. (2005) Atlas of Eh-pH diagrams. Geological Survey of Japan Open File Report #419,

480   102pp.

481   Tebo, B. M., Bargar, J. R., Clement, B. G., Dick, G. J., Murray, K. J., Parker, D., Verity, R., and

482   Webb, S. M., (2004) Biogenic Manganese oxides: properties and mechanisms of

483   formation, Annual Reviews of Earth and Planetary Sciences 32, 287-328.

484   Thomas, E., and Shackleton, N. J. (1996), The Paleocene-Eocene benthic foraminiferal

485   extinction and stable isotope anomalies, Geol. Soc. London, Spec. Publ., 101(1), 401–

486   441.

487 Thompson, P., Cox, D.E., and Hastings, J.B. (1987) Rietveld refinement of Debye- Scherrer

488   synchrotron X-ray data from Al_2O_3. Journal of Applied Crystallography, 20, 79–83.

489 Toby, B.H. (2001) EXPGUI, a graphical user interface for GSAS. Journal of Applied

490   Crystallography, 34, 210-213.

491 Wadsley, A.D. (1955) The crystal structure of chalcophanite, $ZnMn_3O_7{\cdot}3H_2O$. Acta

492   Crystallographica, 8, 165-172.

493 Winguth, A. M. E., Thomas, E., and Winguth, C. (2012), Global decline in ocean ventilation,

494   oxygenation, and productivity during the Paleocene-Eocene Thermal Maximum:

495   Implications for the benthic extinction, Geology, 40(3), 263–266.

496 Zachos et al. (2004) Leg 208: Early Cenozoic Extreme Climates: The Walvis Ridge Transect, 6

497   March–6 May 2003. Proc. ODP, Init. Repts., 208 [Online]. Available from World Wide

498   Web: http://www-odp.tamu.edu/publications/208_IR/208ir.htm, Texas A&M University,

499   College Station TX 77845-9547

500 Zachos, J. C., Röhl, U., Schellenberg, S. A., Sluijs, A., Hodell, D. A., Kelly, D. C., Thomas, E.,

501   Nicolo, M., Raffi, I., Lourens, L. J., McCarren, H., and Kroon, D. (2005), Rapid

502   acidification of the ocean during the Paleocene-Eocene thermal maximum. Science, 308

503   (5728), 1611–5.

504

505
506

507

508 **Figure Captions**

509 **Figure 1** Section of Core 208-1262B-15H recovered during Ocean Drilling Leg 208 (Zachos et

510 al., 2004). The Eocene/Paleocene boundary is at the contact between the light colored

511 calcareous ooze and the dark clay, marking the beginning of the thermal maximum and

512 associated severe carbonate dissolution. The nodule used for the X-ray diffraction study was

513 recovered from the section of the core indicated by the arrow.

514

515 **Figure 2.** Backscattered scanning electron microscope (BSE SEM) images of Mn nodules from

516 ~11 cm above the Eocene/Paleocene boundary in Core 208-1262B-15H. a) Complete nodule

517 measuring ~1.2 mm x 0.6 mm, showing hollow interior; b) Higher magnification image of the

518 nodule wall reveals that the nodule consists almost entirely of ~5 um diameter euhedral, plate-

519 like jianshuiite crystals.

520

521 **Figure 3.** a) Jianshuiite crystals from 9 cm above the P/E contact appear to have "exfoliated",

522 perhaps resulting from delamination caused by cation-exchange. EDS analyses (below image)

523 show that thick "caps" contain predominantly Mn, Mg and O with minor K and Ba (labelled as

524 Ti) (EDS spectrum on lower right), whereas the thin central sheet-like layers contain greater

525 amounts of K and Ca and some Ba (EDS spectrum on lower left). b) BSE image showing a range

526 of particle morphologies, all mainly Mn, O, and Mg, but darker areas are more Al-rich and

527 contain minor Ni and Co.

528

529 **Figure 4.** BSE SEM image of jianshuiite crystals from 32 cm above the P/E contact with

530 calcareous nannofossils: #1: *Coccolithus pelagicus* (a solution-resistant taxon), #2: *Prinsius* sp,.

Page 24

531   #3: possibly *Toweius* sp.. The other rings are probably remnants of more complex placoliths that

532   are partially dissolved (identification by I. Raffi).

533

534   **Figure 5.** BSE SEM image of a nodule from nearby Site 1265 (sample 1265A-18H-CC, earliest

535   Oligocene) composed primarily of calcareous nannofossils with clusters of needle-like crystals

536   of Mn oxide, presumably todorokite.

537

538   **Figure 6.** Final observed (black crosses), calculated (solid line), and difference (solid line

539   below) powder X-ray diffraction patterns from the Rietveld refinement for jianshuiite. The

540   Bragg reflections are marked by the set of small vertical lines

541

542   **Figure 7.** Structure drawing of jianshuiite. Mn-O octahedra are colored dark blue, and Mg

543   cations are shown as small yellow spheres. The water O atoms are indicated by larger light-blue

544   spheres. a) the *c* axis is vertical and b) looking normal to the Mn-O octahedral sheets.

545

546

547

548   Table 1. Final Rietveld refinement parameters for jianshuiite

549   _____

Space Group	R-3
Unit Cell	
a (Å)	7.5409(4)
b (Å)	7.5409(4)
c (Å)	20.8079(14)
V (Å^3)	1024.73(14)
Refinement	
No. of data points	1146
No. of reflections	176
Diffraction range (2θ °)	13.5 – 47.3[a]
No. of variables	41
R(F^2)	0.128
R$_{wp}$	0.0205
χ^2	3.54

550

551   [a] λ = 0.8265(8) Å

552

553   Table 2. Atomic coordinates and isotropic displacement factors for jianshuiite

554   _____

555

Atom	x	y	z	Site occupancy Factor	U_{iso}
Mn	0.7201(6)	0.5793(5)	0.00019(22)	1.0	0.003
Mg	0	0	0.10011(34)	1.073(12)[a]	0.003
O(1)	0.5312(21)	0.6125(22)	0.0493(5)	1.0	0.005
O(2)	0.2315(22)	0.1981(24)	0.0498(5)	1.0	0.005
O(3)	0	0	0.7103(7)	1.0	0.005
O(4)	0.1756(15)	0.9414(17)	0.1678(8)	1.0	0.02116(16)

556   Note: U_{iso} for O1, O2, O3, Mg and Mn atoms were fixed to given values and not refined

557   [a] Site also contains minor Ni, Co, and Ba, but was refined as Mg

558

559

560

561   Table 3. Selected bond lengths for jianshuiite (Å)

562   _____

563

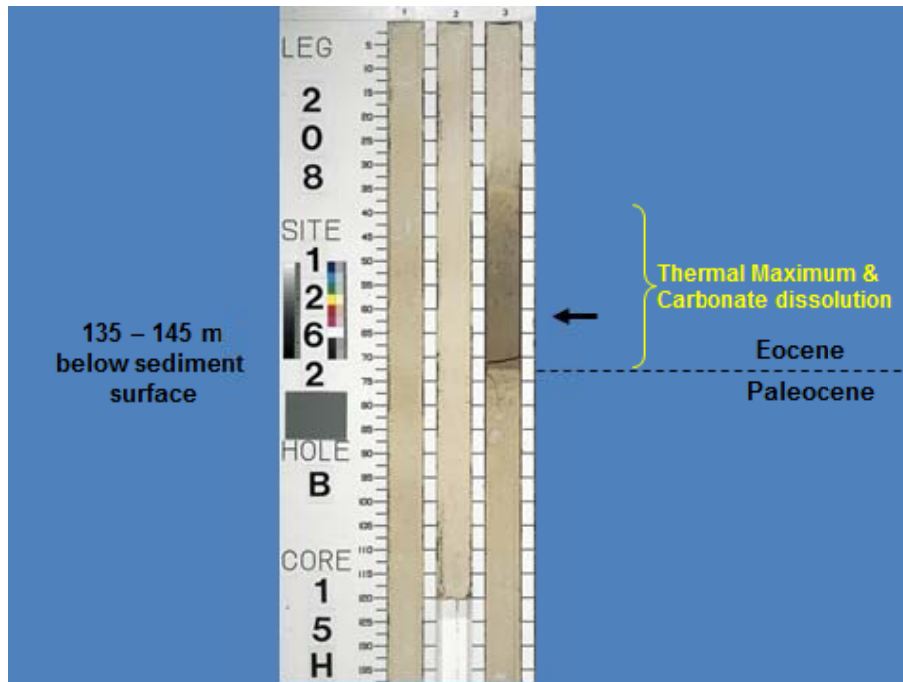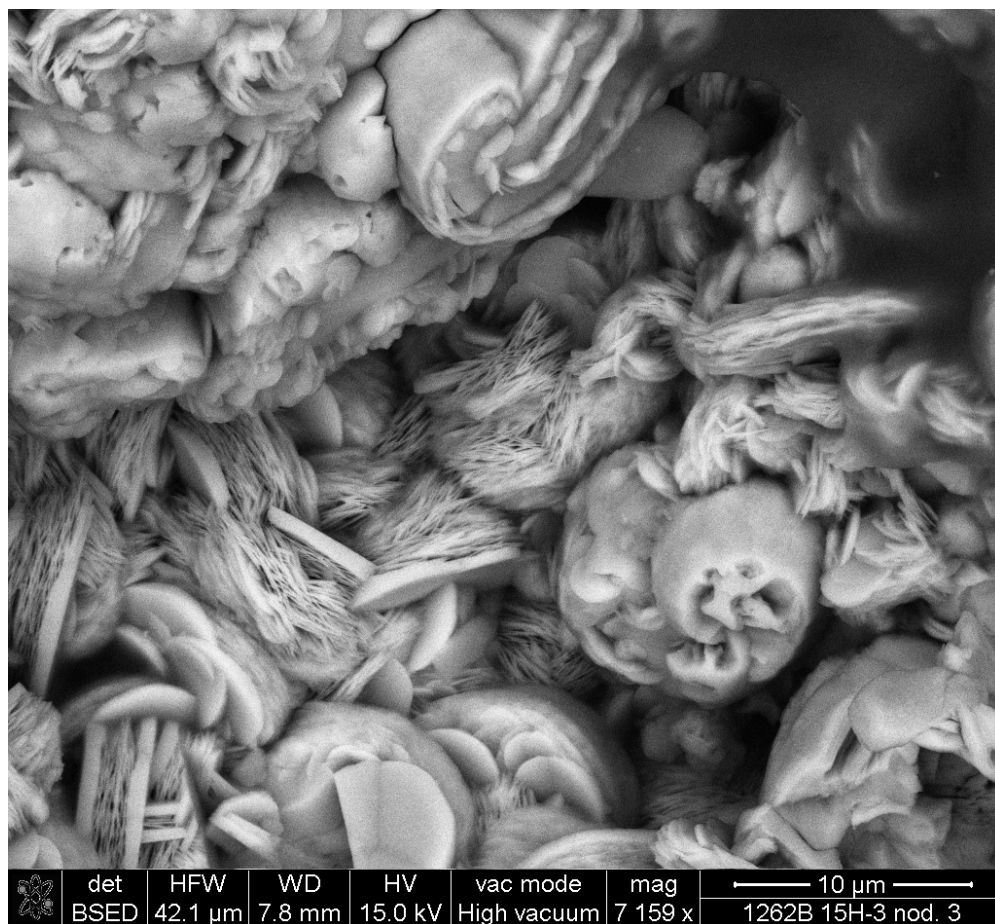| Mn-O(1)	1.869(10)
-O(1)	2.001(13)
-O(1)	1.994(13)
-O(2)	1.976(10)
-O(2)	1.849(14)
-O(3)	1.916(7)
<Mn-O>	1.93
Mg-O(2)	1.941(16) x 3
-O(4)	2.126(13)
<Mg-O>	2.03

564

565

566

567

568

570   Figure 1.

569

| det | HFW | WD | HV | vac mode | mag | ⊢——— 400 μm ———⊣ |
| BSED | 1.47 mm | 7.4 mm | 15.0 kV | High vacuum | 205 x | 1262B 15H-3 nod. 4 |

571

572   Figure 2a.

573
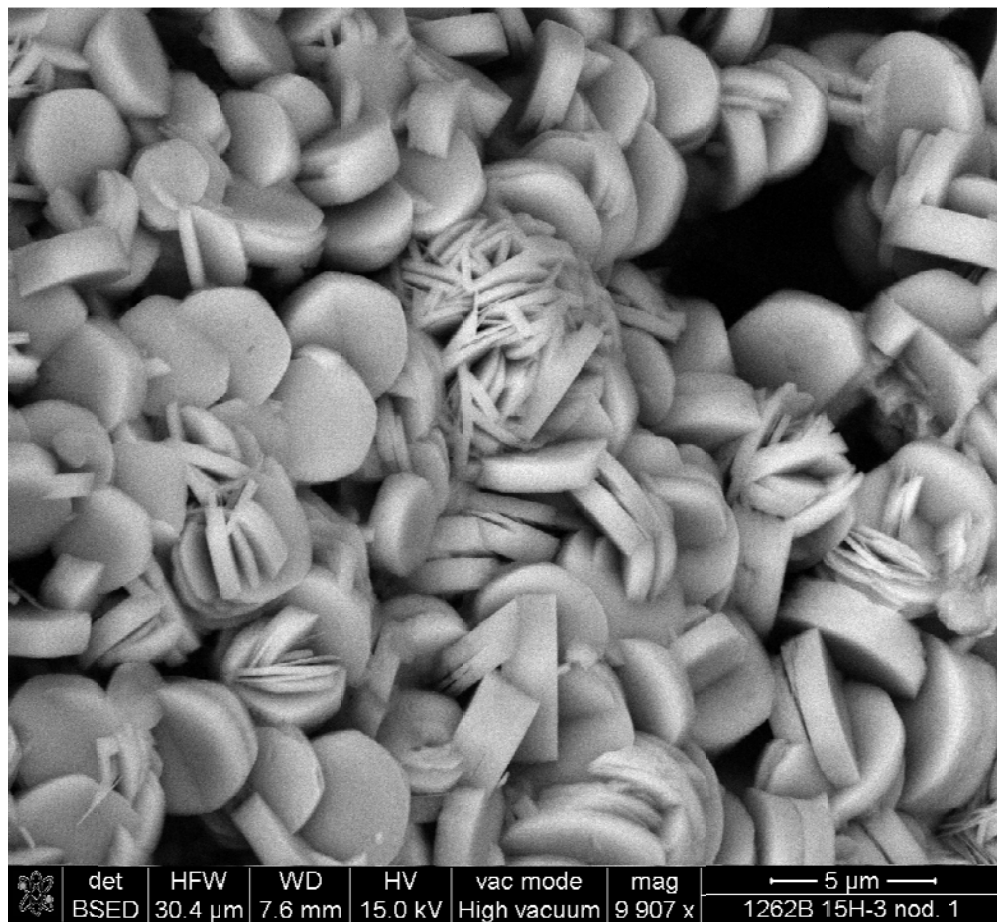
574

575   Figure 2b.

576

577
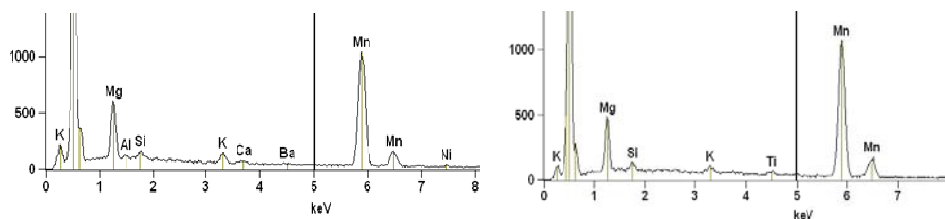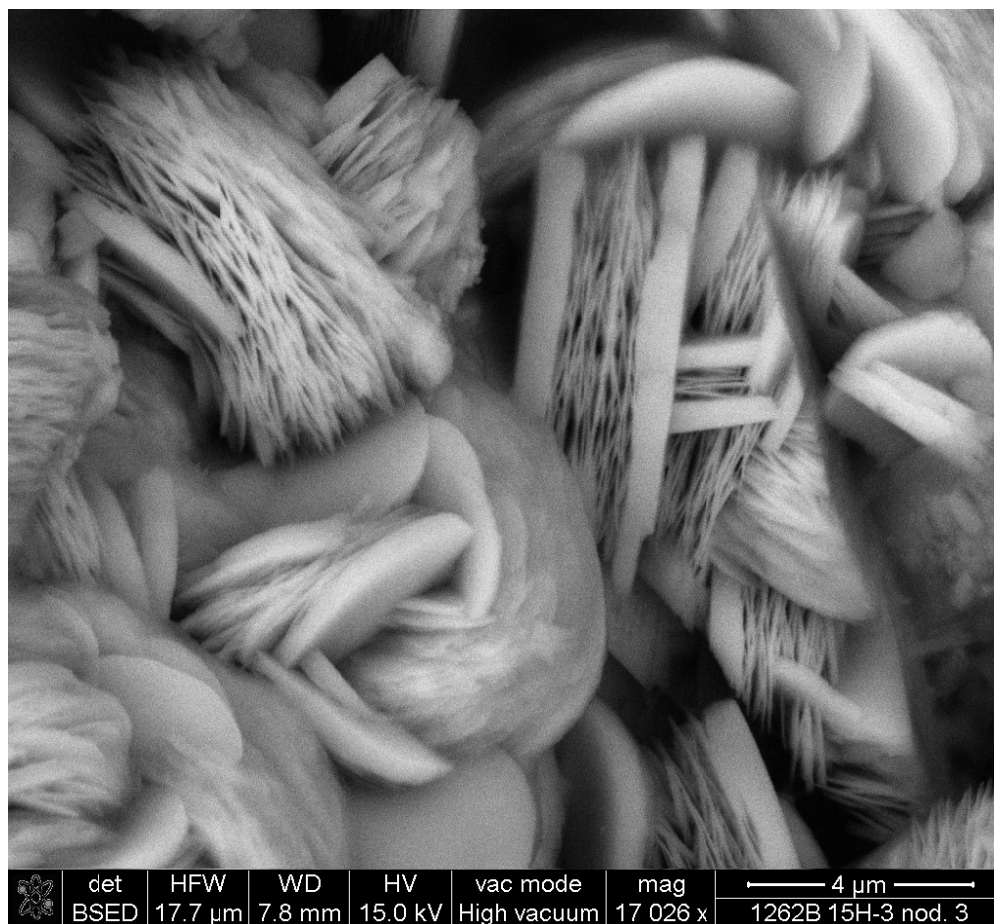
578   Figure 3a

579

580   Figure 3b.

581

582

583

584

585   Figure 4.

586

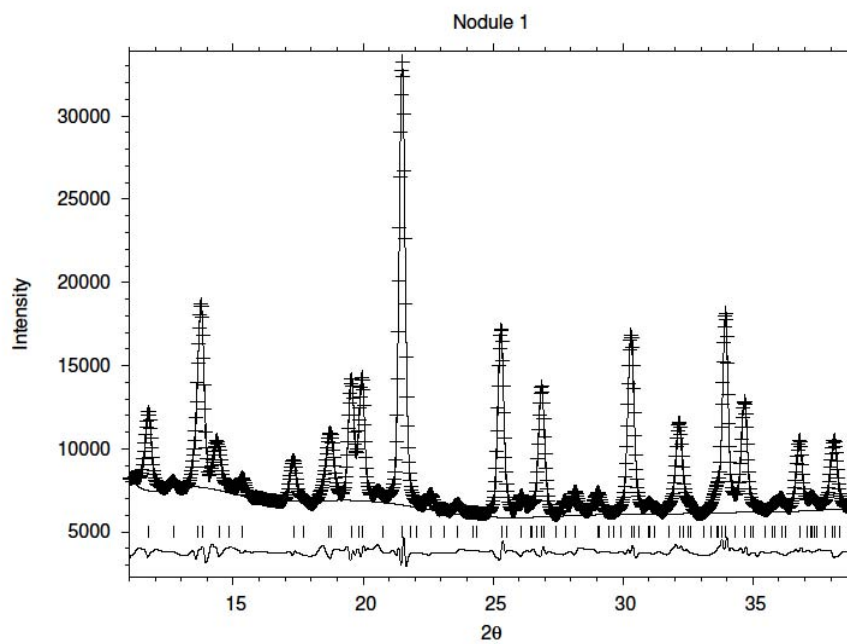| HV	HFW	mag	spot	pressure	WD	vac mode	5 μm
15.0 kV	31.4 μm	9 591 x	4.5	5.61E-9 bar	7.1 mm	High vacuum	Mn nodule C-2
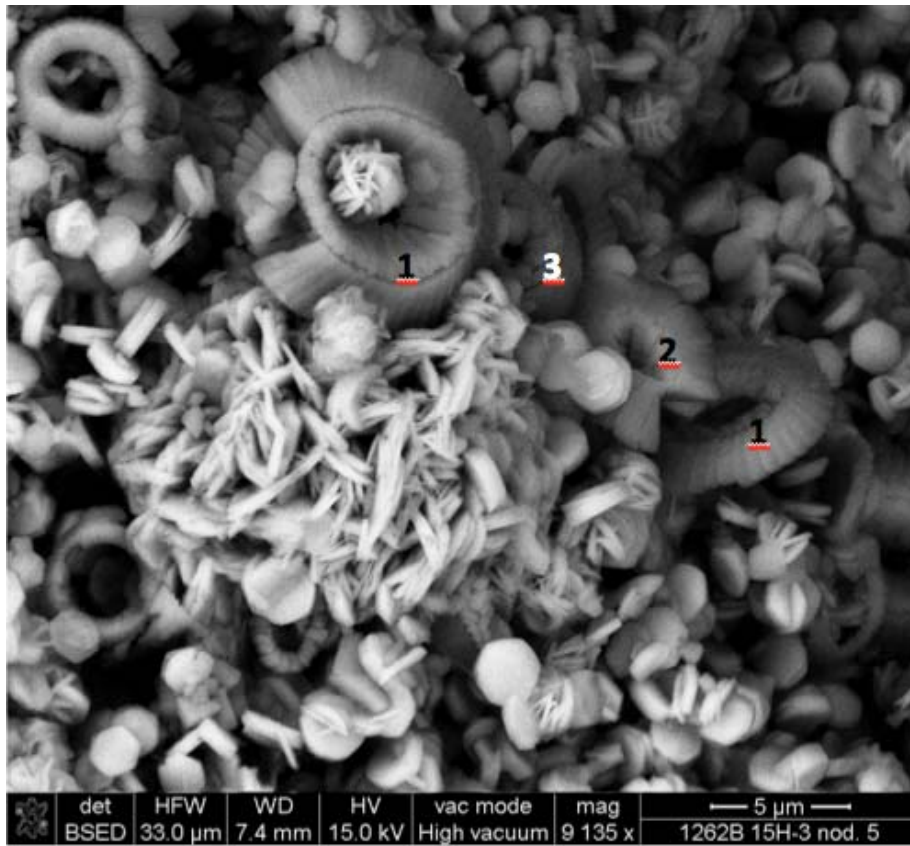
587
588 Figure 5

589

590
591   Figure 6.

592

593

594

595

596

597

598

599

600

601

602

603

604

605

606

607

608

609
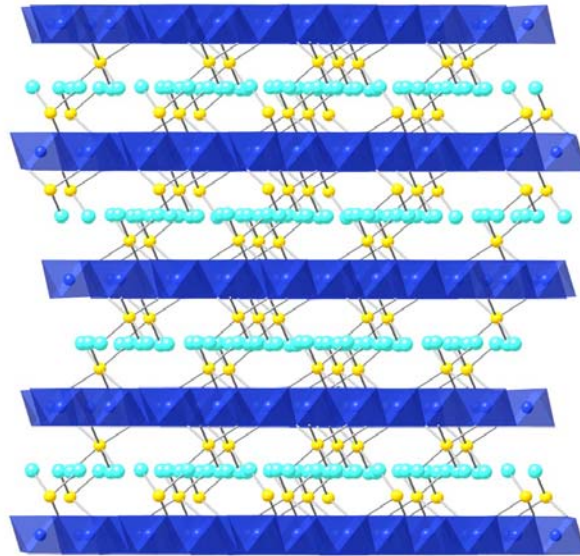
610

611

612

613

614

615   Fig. 7a

616

617

618

619

620

621

622

623

624

625

626

627

628

629

630

631

632

633   Fig. 7b